

LOCAL GROUP DWARF ELLIPTICAL GALAXIES. I. MAPPING THE DYNAMICS OF NGC 205 BEYOND THE TIDAL RADIUS

M. GEHA¹

The Observatories of the Carnegie Institute of Washington, 813 Santa Barbara Street, Pasadena, CA 91101; mgeha@ociw.edu

P. GUHATHAKURTA

UCO/Lick Observatory, University of California, Santa Cruz, 1156 High Street, Santa Cruz, CA 95064; raja@ucolick.org

R. M. RICH

Department of Physics and Astronomy, UCLA, Box 951547, Los Angeles, CA 90095; rmr@astro.ucla.edu

AND

M. C. COOPER

Department of Astronomy, University of California, Berkeley, 601 Campbell Hall, Berkeley, CA 94720-3411; cooper@astron.berkeley.edu

Received 2005 July 20; accepted 2005 September 18

ABSTRACT

NGC 205 is the nearest example of a dwarf elliptical galaxy and the prototype of this enigmatic galaxy class. Photometric evidence suggests that NGC 205, a close satellite of the M31 galaxy, is tidally interacting with its parent galaxy. We present stellar radial velocity measurements out to a projected radius of 20' (5 kpc) in NGC 205 based on Keck DEIMOS multislit spectroscopic observations of 725 individual red giant branch stars. Our kinematic measurements extend from the center out to 6 times the effective radius of NGC 205, well past the expected tidal radius. The contamination in our kinematic sample from M31 field stars is estimated to be a few percent based on maximum likelihood fits to the distribution of stars in position-velocity space. We measure a maximum major-axis rotation speed for the body of NGC 205 of $11 \pm 5 \text{ km s}^{-1}$ and note that this is based on observing a definite turnover in the rotation curve; this is the first dE galaxy in which the maximum rotation velocity has been measured. Combined with the velocity dispersion, we conclude that NGC 205 is supported by a combination of rotation and anisotropic velocity dispersion. At a major-axis distance of 4.5' (1 kpc), the velocity profile of NGC 205 turns over; stars beyond this radius are moving counter to the rotation of the inner part of the galaxy. The turnover radius is coincident with the onset of isophotal twisting and the estimated tidal radius, suggesting that the outer kinematics of NGC 205 is dominated by gravitational interactions with the nearby M31 galaxy. The motion of stars beyond a radius of $\sim 4.5'$ implies that NGC 205 is in a prograde encounter with its parent galaxy, M31.

Key words: galaxies: dwarf — galaxies: individual (NGC 205) — galaxies: interactions — galaxies: kinematics and dynamics

Online material: color figure, machine-readable table

1. INTRODUCTION

NGC 205 is a low-luminosity, early-type dwarf galaxy in the Local Group and one of the brightest nearby examples of a dwarf elliptical (dE) galaxy (see Table 1). A close satellite of the large spiral galaxy Andromeda (M31), NGC 205 has a projected separation from M31 of merely 40', or 8 kpc (Fig. 1); the physical separation between NGC 205 and M31 is estimated to be ~ 40 kpc (Demers et al. 2003; McConnachie et al. 2005). This separation distance is intermediate between that of the Milky Way and its dwarf satellite galaxies Sagittarius (24 kpc; Ibata et al. 1995) and the Large Magellanic Cloud (50 kpc; Freedman et al. 2001). Observational evidence, such as isophotal twisting at large radii (Hodge 1973; Kent 1987; Choi et al. 2002), recent star formation (Peletier 1993; Cappellari et al. 1999), and a steadily increasing velocity dispersion with radius (Bender et al. 1991; Simien & Prugniel 2002), suggests that NGC 205 is tidally interacting with its parent galaxy. However, inside the effective radius, $r_{\text{eff}} = 2.5'$ (0.6 kpc), NGC 205 exhibits regular surface brightness and kinematic profiles typical of a normal dE galaxy. NGC 205 therefore offers a unique opportunity to study the internal dynamics of a

nearby dE galaxy while providing a detailed view of a satellite undergoing disruption.

A crucial question for current galaxy formation theories is to what extent the accretion of dwarf satellite galaxies contributes to the growth of massive galactic halos (Bullock et al. 2000; Font et al. 2005). The M31 galaxy and its associated dwarf satellite system are an excellent laboratory to study this question in detail: M31 is the nearest massive galaxy external to the Milky Way in which current observing techniques are able to resolve individual stars. Ibata et al. (2001) and Ferguson et al. (2002) first detected evidence for tidal streams in the halo of M31 based on wide-area star count maps. Guhathakurta et al. (2004) and Ibata et al. (2004) provided confirmation that the stars in these streams are dynamically related and have a small enough velocity dispersion to have feasibly been stripped from a dwarf-sized galaxy. Meylan et al. (2001) have suggested that the globular cluster G1, one of the brightest globular clusters belonging to M31, is the remnant core of a nucleated dwarf galaxy based on its internal dynamics and stellar populations. From these observations, it is clear that dwarf satellite disruption must have contributed to the buildup of M31's halo; detailed study of current, ongoing interactions between M31 and its satellites should help quantify what fraction of halo material is attributed to this process.

¹ Hubble Fellow.

TABLE 1
NGC 205 AT A GLANCE

Parameter	Value
Name	NGC 205
α (J2000.0)	00 40 22
δ (J2000.0)	+41 41 07
Type.....	dE5
Distance (kpc)	824
m_B	9.9
$M_{B,0}$	-15.0
ϵ	0.43
$\mu_{B,\text{eff}}$ (mag arcsec $^{-2}$)	23.7
r_{eff} (arcmin)	2.5
r_{eff} (kpc)	0.6
r_{tidal} (arcmin)	4.5
r_{tidal} (kpc)	1.1

NOTES.—The right ascension, declination, and morphological type of NGC 205 are taken from the NASA/IPAC Extragalactic Database. We adopt the distance to NGC 205 determined by McConnachie et al. (2005). The apparent magnitude, effective surface brightness, effective radius, and ellipticity are determined from B -band photometry from Choi et al. (2002). The ellipticity ϵ is the average value measured between 0'.5 and 5'. The absolute magnitude is calculated assuming an extinction of $A_B = 0.27$ from Schlegel et al. (1998). The tidal radius r_{tidal} is calculated based on the assumptions outlined in § 4. Units of right ascension are hours, minutes, and seconds, and units of declination are degrees, arcminutes, and arcseconds.

Galaxy formation scenarios for the origin of dE galaxies lie broadly in two very distinct categories: (1) dE galaxies as old, primordial objects and (2) dE galaxies having recently evolved or transformed from a progenitor galaxy population (Dekel & Silk 1986; Moore et al. 1998; Mayer et al. 2001; Mastropietro et al. 2005). Dwarf elliptical galaxies are highly clustered (Binggeli et al. 1988); the majority of dE galaxies in the local universe are found in dense galaxy clusters. Kinematic studies of dE galaxies in the Virgo and Fornax Clusters suggest a large range in their kinematic properties, from rotationally supported galaxies to dE galaxies with no detectable major-axis rotation (Geha et al. 2003; De Rijcke et al. 2001; van Zee et al. 2004). These results, in particular the abundance of dE galaxies with a complete lack of rotation, have so far been difficult to explain in the context of current formation models. The three bright Local Group dE satellites NGC 205, NGC 147, and NGC 185 provide an excellent opportunity to study dE kinematics in greater detail and to larger radii than their cluster counterparts. In this paper, we present kinematics for the brightest of the Local Group dE galaxies, NGC 205.

The absolute magnitude of NGC 205 is $M_V = -16.5$. It has a nearly exponential surface brightness profile (Choi et al. 2002), characteristic of dE galaxies. As a result, NGC 205 has a far more diffuse appearance than the other bright M31 satellite galaxy, M32, which has a similar absolute magnitude but is classified as a compact elliptical galaxy. Near the center of this galaxy, inside a radius of 1' (0.24 kpc), NGC 205 contains dust (Haas 1998), atomic and molecular gas (Welch et al. 1998; Young & Lo 1997), and a number of OB associations implying a recent episode of star formation in the past 100 Myr (Peletier 1993; Lee 1996). Beyond this radius, NGC 205 is gas- and dust-free and is composed of an intermediate stellar population (Demers et al. 2003), typical for similarly sized dE galaxies in the Virgo Cluster (Geha et al. 2003).

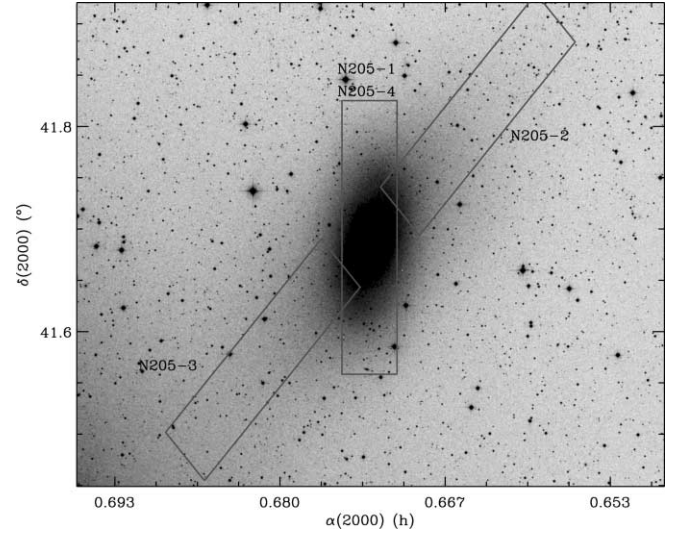


FIG. 1.—Digitized Sky Survey image of NGC 205. The placement of the four DEIMOS slit masks (N205-1 through N205-4) is shown. The image is 42' \times 28'; north is up, and east is to the left. The disk of M31 can be seen in the bottom left (southeast) corner of the image. [See the electronic edition of the *Journal* for a color version of this figure.]

Early dynamical studies suggested that NGC 205 had negligible internal rotation velocity. Dynamical measurements by Bender et al. (1991) placed an upper limit on the rotation velocity of $1.5 \pm 0.8 \text{ km s}^{-1}$ at $\sim r_{\text{eff}}$. Combined with observations of two other Local Group dE galaxies, this established the paradigm that dE galaxies are supported primarily by anisotropic velocity dispersions. However, Simien & Prugniel (2002) more recently measured the major-axis rotation of NGC 205 out to twice the effective radius, measuring a rotation speed of $13 \pm 2 \text{ km s}^{-1}$. The central velocity dispersion of NGC 205 has a value of $16 \pm 4 \text{ km s}^{-1}$ (Peterson & Caldwell 1993; Carter & Sadler 1990), increasing with radius to 42 km s^{-1} at 2' (Bender et al. 1991) and 50 km s^{-1} at 5' (Simien & Prugniel 2002). Assuming an isotropic spheroid model, Bender et al. (1991) inferred a mass-to-light ratio of $M/L \sim 7$ for NGC 205, similar to those inferred for a sample of Virgo and Fornax Cluster dE galaxies based on more sophisticated dynamical modeling (Geha et al. 2002; De Rijcke et al. 2001). These ratios are consistent with that of a modestly old stellar population with no dark matter. This lack of dark matter in the inner region is in stark contrast to the much larger M/L s inferred for fainter dwarf spheroidal (dSph) galaxies in the Local Group, such as the Draco and Ursa Minor dSph galaxies, which appear to be dark-matter-dominated even in their central regions (Kleyna et al. 2003).

Integrated-light spectroscopy cannot probe the kinematics of dE galaxies much beyond the effective radius due to their characteristic low surface brightness ($\mu_{V,\text{eff}} = 23 \text{ mag arcsec}^{-1}$). Unlike dwarf irregular galaxies, dE galaxies are devoid of gas at large radii, so their outer kinematics cannot be studied via H I gas dynamics. Other kinematical probes exist at large radii, such as globular clusters (Beasley et al. 2006) and planetary nebulae (Corradi et al. 2005), but their small numbers make these poor kinematic tracers. The proximity of NGC 205 presents a unique opportunity to study the dynamics of a dE galaxy out to much larger radii than possible in more distant systems, via spectroscopy of individual red giant branch (RGB) stars.

In this paper, we present accurate radial velocities for 725 RGB stars in the Local Group dE galaxy NGC 205 measured via Keck DEIMOS multislit spectroscopy. We present dynamics of

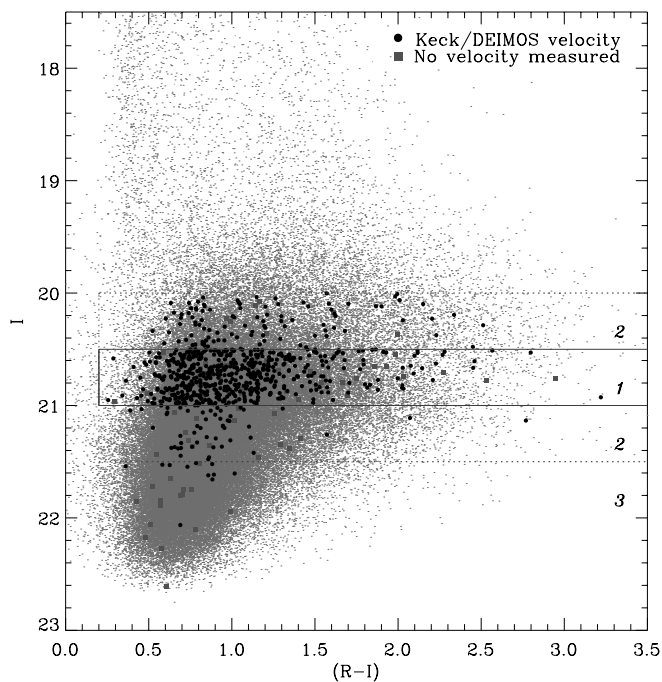


FIG. 2.—Color-magnitude diagram based on Demers et al. (2003) R - and I -band CFH12K photometry in a $42' \times 28'$ region centered on NGC 205. Large symbols indicate objects targeted for DEIMOS spectroscopy in this study: circles represent targets with measured velocities, and squares represent targets for which no velocity could be measured. The numbered boxes indicate the location of our (1) primary, (2) secondary, and (3) tertiary spectroscopic priorities.

this galaxy well beyond the inferred tidal radius, twice the radial extent of previous measurements. This paper is organized as follows: In § 2, we discuss target selection for our DEIMOS slit masks, the observing procedure, and data reduction. In § 3, a detailed kinematic analysis of NGC 205 is presented along with a maximum likelihood estimate of the kinematic contamination from stars in M31. Finally, in § 4, we discuss the implications of our kinematic observations for the tidal interaction between NGC 205 and M31.

Throughout this paper we adopt a distance modulus to NGC 205 of $(m - M)_0 = 24.58 \pm 0.07$, i.e., a distance of 824 ± 27 kpc, as determined by McConnachie et al. (2005) via the tip of the RGB method; this places NGC 205 40 kpc farther than its parent galaxy, M31.

2. DATA

2.1. Target Selection

Stars were selected for spectroscopy according to their probability of being an RGB star in NGC 205. Stars were selected based on Canada-France-Hawaii Telescope CFH12K mosaic imaging in the R and I bands, kindly provided by S. Demers et al. (2003, private communication). The CCD mosaic covers a $42' \times 28'$ region centered on NGC 205 with $0''.206$ pixels. The images were obtained in subarcsecond seeing conditions. Stellar photometry from these images extends 2 mag below the tip of the RGB. The color-magnitude diagram for this region is shown in Figure 2. A broad RGB is seen extending to very red colors ($R - I > 3.0$); the reddest of these stars are likely to be metal-rich/reddened M31 disk RGB contaminants (Demers et al. 2003). The vertical ridge near $(R - I) = 0.2$ is due to foreground Milky Way stars. The spatial distribution of stars is shown in Figure 3.

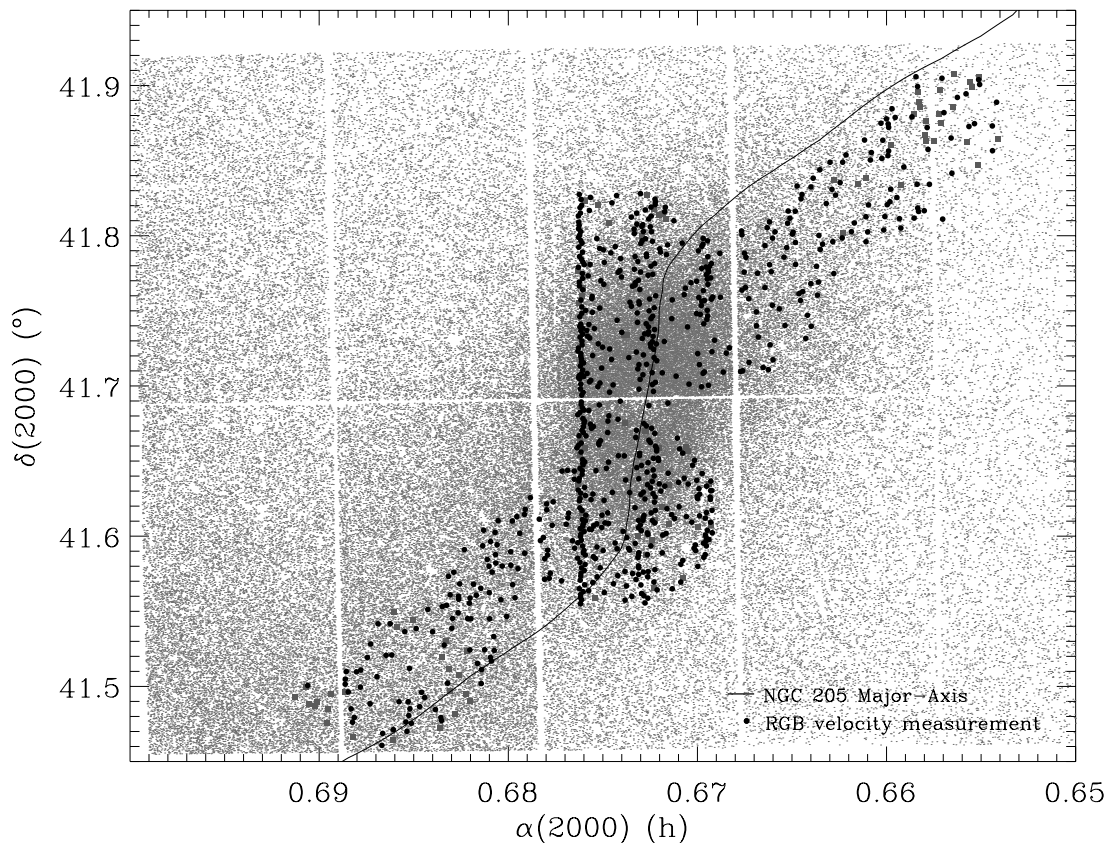


FIG. 3.—Spatial distribution of stars in NGC 205 (small gray dots) from Demers et al. (2003) photometry. Large circles indicate objects targeted for DEIMOS spectroscopy; the tiered pattern of slitlets can be seen in the central mask. The solid curve shows the major axis of NGC 205 determined from Choi et al. (2002) photometry.

TABLE 2
KECK DEIMOS MULTISLIT MASK OBSERVING PARAMETERS

Mask Name	α (J2000.0)	δ (J2000.0)	P.A. (deg)	t_{exp} (s)	Number of Slits	Useful Spectra (%)
N205-1	00 40 27.4	+41 41 30.5	0	3600	184	91
N205-2	00 39 50.5	+41 48 41.8	-45	3600	185	85
N205-3	00 40 53.0	+41 40 53.0	-45	3600	193	84
N205-4	00 40 27.4	+41 41 30.5	0	3600	320	88

NOTES.—Right ascension, declination, position angle, and total exposure time for each Keck DEIMOS slit mask. The final two columns refer to the total number of slitlets on each mask and the percentage of those slitlets for which a redshift was measured. Units of right ascension are hours, minutes, and seconds, and units of declination are degrees, arcminutes, and arcseconds.

The gaps between the CFH12K CCD chips are $\sim 7''$ wide. The apparent hole in the stellar density map near the center of NGC 205 is due to crowding; the stellar density increase in the lower left corner is due to the presence of field RGB stars belonging to M31.

The absolute magnitude of the RGB is $M_I \sim -4$. At the assumed distance of NGC 205, the apparent magnitude of this stellar population is $I \sim 21$. Since metallicity variations within NGC 205 will cause a spread in the colors of its RGB stars, we select spectroscopic targets based primarily on apparent magnitude. Highest priority in the spectroscopic target list was assigned to stars in the range $20.5 \leq I \leq 21.0$. Second priority was given to stars in the range $20.0 \leq I < 20.5$ and $21.0 < I \leq 21.5$; lowest priority was assigned to objects $I > 21.5$. To minimize Galactic foreground contamination, targets were required to have $(R - I) > 0.2$. Stars with photometric errors larger than $\sigma_I > 0.1$ were rejected, as were stars having neighbors of equal or greater brightness within a radius $r < 4''$. The photometric criteria used for spectroscopic target selection are shown in Figure 2.

2.2. DEIMOS Multislit Mask Design

Four multislit masks were observed on the nights of 2003 September 30 and October 1 with the Keck II 10 m telescope and DEIMOS (Faber et al. 2003). Three of the four masks (N205-1, N205-2, and N205-3) were designed to be observed in a conventional mode, while a fourth mask was designed to have multiple tiers of spectra, as described in § 2.2.2. Science exposures for all four masks were 3×1200 s per mask; the average seeing FWHM during the spectroscopic observations was $0''.7$.

In Figure 1, the placement of the four DEIMOS slit masks is shown relative to a Digitized Sky Survey image of NGC 205. Each DEIMOS multislit mask covers a rectangular area of $\approx 16' \times 4'$. Two slit masks (N205-1 and N205-4) were positioned on the center of NGC 205 with the long axis of the mask along the major axis of the galaxy. The centers of masks N205-2 and N205-3 were placed $10'$ to the southeast and northwest of NGC 205, respectively. The long axes of these two masks were roughly placed along the direction of tidal distortion. The direction of tidal distortion was determined from surface brightness ellipse fitting by Choi et al. (2002) based on wide-field B -band photometry. The locus of semimajor axes of the ellipse fitting forms a gentle S-curve, which we plot in Figure 3 and refer to as the major axis of NGC 205 (see § 3). Slitlets in each mask have the same position angle as the overall mask; i.e., we did not use tilted slits. In Table 2, we list the observing details for each mask.

2.2.1. Conventional Masks

The three conventional DEIMOS slit masks (N205-1, N205-2, and N205-3) were designed to be observed with the 1200 line mm^{-1}

grating covering a wavelength region of 6400–9100 Å. The spectral dispersion of this setup is 0.33 Å , and the resulting spectral resolution, taking into account the anamorphic distortion factor of 0.706, is 1.37 Å (FWHM). This wavelength range includes the Ca II triplet lines, which are expected to be strong in absorption for our targeted RGB stars. Slitlets were $0''.7$ wide to match the typical seeing conditions while maintaining good wavelength resolution. The spatial scale is $0''.12 \text{ pixel}^{-1}$, and the spectral dispersion is $0.33 \text{ Å pixel}^{-1}$. To allow adequate sky subtraction, the minimum slit length was $5''$; the minimum spatial separation between slit ends was $0''.4$ (3 pixels).

Using the above input parameters and the target list described in § 2.1, slit masks were created using the DEIMOS DSIMULATOR² slit mask design software. For each slit mask the software starts with the highest priority input targets and automatically fills in the mask area to the extent possible, filling in the remaining space on the slit mask with lower priority targets. An average of nearly 200 slitlets were placed on each mask (see Table 2). A handful of targets were deliberately included on multiple masks. These overlapping targets are used to quantify measurement errors in § 2.4.

2.2.2. Multitier Masks

The DEIMOS slit mask N205-4 was designed for use with a blocking filter centered on the Ca II triplet region. The blocking filter allows multiple tiers of slitlets to be placed on a single mask, increasing the observing efficiency by a factor of 2–3 over conventional DEIMOS masks. The Ca II blocking filter has a central wavelength of 8550 Å and is 350 Å wide. In combination with the 831 line mm^{-1} grating, the spectral dispersion of this setup is 0.47 Å , and the resulting spectral resolution is 1.96 Å (FWHM). Two and a half tiers of spectra are possible without significant overlap in the wavelength region of 8450–8850 Å. Three full tiers of spectra are not possible, because the DEIMOS field of view is narrower in the middle than at the ends. The width and typical length of the slitlets are the same as for the conventional masks described above. This mask was designed by running DSIMULATOR three times over the mask. In each pass, slitlets were placed on targets in a row running along the spatial axis of the mask to maximize the number of slitlets. For each pass of DSIMULATOR, the region of the CCD detector plane occupied by the spectra of all the slitlets was calculated, the spectroscopic targets in this region were excluded, and the resulting target list was fed into the next pass. A total of 332 slitlets were placed on the N205-4 mask. The tier pattern of slitlets can be seen in the spatial distribution of targets in Figure 3.

² Available at http://www.ucolick.org/~phillips/deimos_ref/masks.html.

2.3. Data Reduction

Spectra from the three conventional DEIMOS multislit masks were reduced using the *spec2d* software pipeline (ver. 1.1.4) developed by the DEEP2 team at the University of California, Berkeley, for that survey. A detailed description of the reductions can be found in M. C. Cooper et al. (2006, in preparation). Briefly, the flat-field exposures are used to rectify the curved raw spectra into rectangular arrays by applying small shifts and interpolating in the spatial direction. A one-dimensional slit function correction and two-dimensional flat-field and fringing correction are applied to each slitlet. Using the DEIMOS optical model as a starting point, a two-dimensional wavelength solution is determined from the arc lamp exposures with residuals of order 0.01 \AA . Each slitlet is then sky-subtracted, exposure by exposure, using a B-spline model for the sky. The individual exposures of the slitlet are averaged with cosmic-ray rejection and inverse-variance weighting. Finally, one-dimensional spectra are extracted for all science targets using the optimal scheme of Horne (1986) and are rebinned into logarithmic wavelength bins with $15 \text{ km s}^{-1} \text{ pixel}^{-1}$. Sample one-dimensional spectra are shown in Figure 4.

Spectra from the multitier mask N205-4 were reduced using a combination of IRAF multislit and long-slit tasks similar to the method described in Geha et al. (2002). The flat-field exposure for this mask was used to trace the ends of each slitlet. The *apall* task was used in “strip” mode to extract and rectify two-dimensional rectangular strips for each slitlet; a similar extraction was applied to the arc lamp calibration and science frames. Data reduction proceeded on these rectified strips. Each strip was divided by its corresponding normalized flat-field image. Individual science exposures were cleaned of cosmic rays and combined. A wavelength solution was determined for each slitlet from the combined KrArNeXe arc lamp spectrum and was applied to the data. One-dimensional spectra were then extracted from each strip and rebinned into logarithmic wavelength bins with $20 \text{ km s}^{-1} \text{ pixel}^{-1}$.

2.4. Radial Velocities

Radial velocities were measured for spectra extracted from the four DEIMOS masks by cross-correlating the observed spectra with a series of high signal-to-noise ratio stellar templates originally created for the Sloan Digital Sky Survey covering a wide range of stellar spectral types (M. C. Cooper et al. 2006, in preparation). These templates were rebinned to match the final wavelength resolution of the observations of 15 and $20 \text{ km s}^{-1} \text{ pixel}^{-1}$ for the conventional and multitier masks, respectively. The science and template spectra were continuum-subtracted; the template was then shifted and scaled to minimize the reduced χ^2 . A heliocentric correction was applied to all the measured radial velocities. The fitted velocities were visually inspected and assigned a quality code to indicate the reliability of the measured redshift and the overall quality of the spectrum.

Radial velocities for individual stars were successfully measured for 769 of the 869 extracted spectra. Of the 100 spectra for which we did not measure a redshift, 51 spectra were unusable due to bad columns or vignetting, and 49 spectra had insufficient signal-to-noise ratios to determine a redshift. Of the spectra with measured velocities, three were background galaxies and 41 were duplicate measurements. Duplicate measurements are used to estimate our velocity error bars, as discussed below. The final sample consists of 725 unique stellar radial velocity measurements.

We estimate the accuracy of our radial velocity measurements via repeat measurements of stars across the four observed masks. Twenty-nine duplicate stars were observed across the three con-

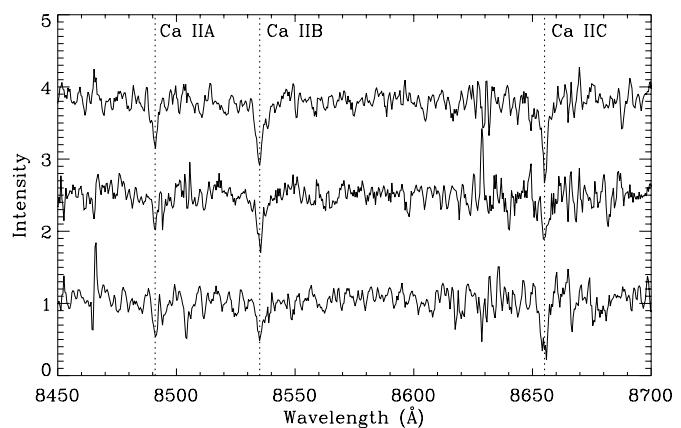


FIG. 4.—Representative one-dimensional Keck DEIMOS spectra of RGB stars in NGC 205 centered on the Ca II region. We compare spectra from three slitlets in the inner region of NGC 205.

ventional masks. Twelve stars on the multitier mask were duplicated on the conventional masks. The rms radial velocity difference between pairs of measurements for stars on the conventional masks is 16.3 km s^{-1} . Assuming that the measurement uncertainty is the same for each member of the pair, the radial velocity error for an individual measurement is $\sqrt{2}$ times smaller than the rms of the difference, or 11.5 km s^{-1} . The rms difference between the conventional and multitier masks is 21.7 km s^{-1} ; this rms difference is larger than the conventional masks due to lower spectral resolution and the smaller available wavelength region in the multitier design. Assuming velocity errors between the conventional and multitier masks add in quadrature, the radial velocity error on individual multitier measurements is 18.4 km s^{-1} . Velocity measurements for individual stars are listed in Table 3.

3. RESULTS

The measured velocities of individual stars allow us to probe the dynamics of NGC 205 to much larger radii than possible via integrated-light spectroscopy. In Figure 5, we show the distribution of radial velocities of individual RGB stars in the four Keck DEIMOS slit masks. The distribution of velocities in slit masks N205-1 and N205-4 is centered on the systemic velocity of NGC 205. The systemic velocity of NGC 205 is $v_{\text{sys}} = -246 \pm 1 \text{ km s}^{-1}$ based on the median velocity of stars with semimajor axis distances less than $5'$. The two slit masks off-center from NGC 205 show skewed velocity distributions. The mask N205-2, placed to the northwest of NGC 205 on the far side from M31, is skewed toward more positive velocities than the NGC 205 systemic velocity; mask N205-3, to the southeast of NGC 205 nearer to M31, has more negative velocities relative to the NGC 205 systemic velocity. To illustrate this observation, we fit a Gaussian profile to the combined distribution of velocities (Fig. 5, bottom). The fitted Gaussian has a central velocity of -246 km s^{-1} , in agreement with the systemic velocity of NGC 205 measured above, and a velocity width of 42 km s^{-1} , in agreement with the average velocity dispersion of NGC 205 measured by Simien & Prugniel (2002). In the top panels of Figure 5 we plot the scaled Gaussian profile; the excess of stars in masks N205-2 and N205-3 is clearly visible to the right and left, respectively, of the main velocity peak. In all four masks, there are a small number of stars with velocities less negative than that of NGC 205 due to foreground contamination, while stars with more negative velocities are primarily M31 halo stars whose systemic velocity is -300 km s^{-1} . We estimate M31 contamination fractions in our sample in § 3.2.

TABLE 3
VELOCITY MEASUREMENTS FOR INDIVIDUAL STARS IN NGC 205

Name	α (J2000.0)	δ (J2000.0)	I (mag)	$(R-I)$ (mag)	v (km s ⁻¹)	v_{err} (km s ⁻¹)	S/N	Mask
2186.....	00 39 15.0	+41 53 19.8	20.7	1.03	-195.9	11.5	15.7	N205-2
2196.....	00 39 15.9	+41 52 23.0	20.7	0.89	-309.8	11.5	11.7	N205-2
2272.....	00 39 23.6	+41 50 29.5	20.7	0.93	-213.8	11.5	13.6	N205-2
2441.....	00 39 25.3	+41 48 39.8	20.9	0.84	-240.8	11.5	9.0	N205-2
2658.....	00 39 20.3	+41 52 21.7	20.9	1.30	-162.9	11.5	12.6	N205-2
2681.....	00 39 18.5	+41 54 13.7	21.0	0.91	-261.8	11.5	10.5	N205-2
2770.....	00 39 15.8	+41 51 23.7	21.0	1.07	-225.8	11.5	9.8	N205-2
2805.....	00 39 20.9	+41 53 40.0	21.1	0.99	-291.8	11.5	10.1	N205-2
3047.....	00 39 25.1	+41 52 54.9	21.2	0.77	-174.9	11.5	7.7	N205-2
3234.....	00 39 22.5	+41 53 31.4	21.4	0.69	-96.9	11.5	7.1	N205-2
3238.....	00 39 23.7	+41 51 54.1	21.4	0.66	-288.8	11.5	7.3	N205-2
3239.....	00 39 18.3	+41 54 02.4	21.3	0.79	-171.9	11.5	8.7	N205-2
3279.....	00 39 19.3	+41 52 28.5	21.3	0.90	-165.9	11.5	7.9	N205-2
3804.....	00 39 25.5	+41 54 17.3	21.6	0.86	-318.8	11.5	7.0	N205-2
4716.....	00 39 30.2	+41 50 03.2	20.1	1.87	-393.7	11.5	30.8	N205-2
4773.....	00 39 57.6	+41 43 02.7	20.6	0.29	-219.8	11.5	18.6	N205-2
4832.....	00 40 02.2	+41 42 56.5	20.8	0.64	-168.9	11.5	21.9	N205-2
4914.....	00 39 50.4	+41 49 56.8	20.5	0.71	-201.9	11.5	18.9	N205-2
5002.....	00 39 36.5	+41 48 13.7	20.6	0.78	-516.6	11.5	16.3	N205-2
5096.....	00 40 02.9	+41 45 56.0	20.5	1.30	-165.9	11.5	17.8	N205-2
5100.....	00 39 58.3	+41 48 33.2	20.5	1.35	-162.9	11.5	18.0	N205-2
5109.....	00 39 52.1	+41 49 38.8	20.5	1.01	-267.8	11.5	18.9	N205-2
5123.....	00 39 57.2	+41 48 09.3	20.6	0.97	-234.8	11.5	17.9	N205-2

NOTES.—Star names, positions, and magnitudes are taken from Demers et al. (2003). We list the heliocentric radial velocity (v), the velocity error (v_{err}), the median per pixel signal-to-noise ratio (S/N), and the DEIMOS mask name for each star. Velocity error bars were determined from measurement overlaps for each mask as discussed in § 2.4. We also list the median per pixel S/N value for each slitlet in the wavelength range 8000–9000 Å and refer the reader to K. M. Gilbert et al. (2006, in preparation) for a discussion of velocity errors for individual slitlets based on the S/N. Units of right ascension are hours, minutes, and seconds, and units of declination are degrees, arcminutes, and arcseconds. Table 3 is published in its entirety in the electronic edition of the *Astronomical Journal*. A portion is shown here for guidance regarding its form and content.

A semimajor axis distance is assigned to each slitlet based on its minimum distance to the major axis of NGC 205. The major axis of NGC 205 is shown in Figure 3 and was determined from surface brightness ellipse fitting by Choi et al. (2002) based on wide-field B -band images of NGC 205, corrected for the underlying light of M31. For each slitlet, we determine its minimum distance to the major axis (Fig. 3) and assign the semimajor axis length (a) at the point. Although there are alternative methods to assign this distance (e.g., the semimajor distance corresponding to the nearest elliptical isophote), this method most closely resembles integrated-light spectroscopy of more distant dE galaxies to which we compare our results.

3.1. The Velocity Profile of NGC 205

In Figure 6, we present the major-axis velocity profile for NGC 205 determined from the combined velocity measurements of RGB stars. Individual stellar velocity measurements are shown in the top panel of this figure. To determine the ensemble major-axis velocity profile, individual measurements were binned into minimum 1' radial bins with 25 or more stars per bin. The velocity in each bin was determined by simultaneously fitting a double Gaussian profile to the distribution of stars in that bin. To account for contamination from M31 stars, one of the two fitted Gaussian profiles had a fixed mean and velocity width of -300 and 150 km s⁻¹, respectively, corresponding to best estimates for M31's halo (see § 3.2). We fit for the width and mean of the second Gaussian profile to determine both the velocity and velocity dispersion of NGC 205 in each radial bin. The relative height of these two profiles is fixed based on the M31 contamination fraction determined by maximum likelihood fitting in § 3.2. We have also run fits in which the contamination fraction is a free

parameter, which does not change the resulting profile appreciably. The resulting velocity and velocity dispersion profile as a function of radius is shown in Figure 6 (*middle and bottom*). The velocity dispersion profile is determined using a coarser binning scheme of 50 or more stars per radial bin. Error bars were computed based on number statistics in each radial bin that dominate over the radial velocity measurement errors of individual stars. We list the velocity and velocity dispersion as a function of semimajor axis distance, right ascension, and declination in Table 4.

We determine the maximum major-axis rotation velocity, v_{max} , for NGC 205 by differencing the maximum/minimum velocity in the upper left and lower right quadrants of Figure 6 and dividing this number by 2. The maximum rotation velocity for NGC 205 is $v_{\text{max}} = 11 \pm 5$ km s⁻¹. The peak rotation velocity occurs at slightly different radii on either side of the galaxy, with an average radius of $r_{\text{max}} = 4'.5$ (1.1 kpc). Our value is somewhat smaller than, but within the 1 σ error bars of, the value measured by Simien & Prugniel (2002) of 13 ± 2 km s⁻¹ at $r = 4'$ based on integrated-light measurements. The Simien & Prugniel data hint at a flattening in the velocity profile, but the integrated-light data are noisy at these large radii. We observe this turnover conclusively and note that v_{max} is the physical, rather than an observational, maximum rotation velocity. Previous observations of dE galaxies have not reached sufficient radii to observe a definite turnover in the rotation curve; this is the first dE galaxy in which the *maximum* rotation velocity has been measured.

We plot the ratio of the maximum rotation velocity to the average velocity dispersion (v_{max}/σ) versus ellipticity in Figure 7. We assume an ellipticity for NGC 205 of $\epsilon = 0.43$ (Choi et al. 2002) and a velocity dispersion of $\sigma = 35 \pm 5$ km s⁻¹ determined

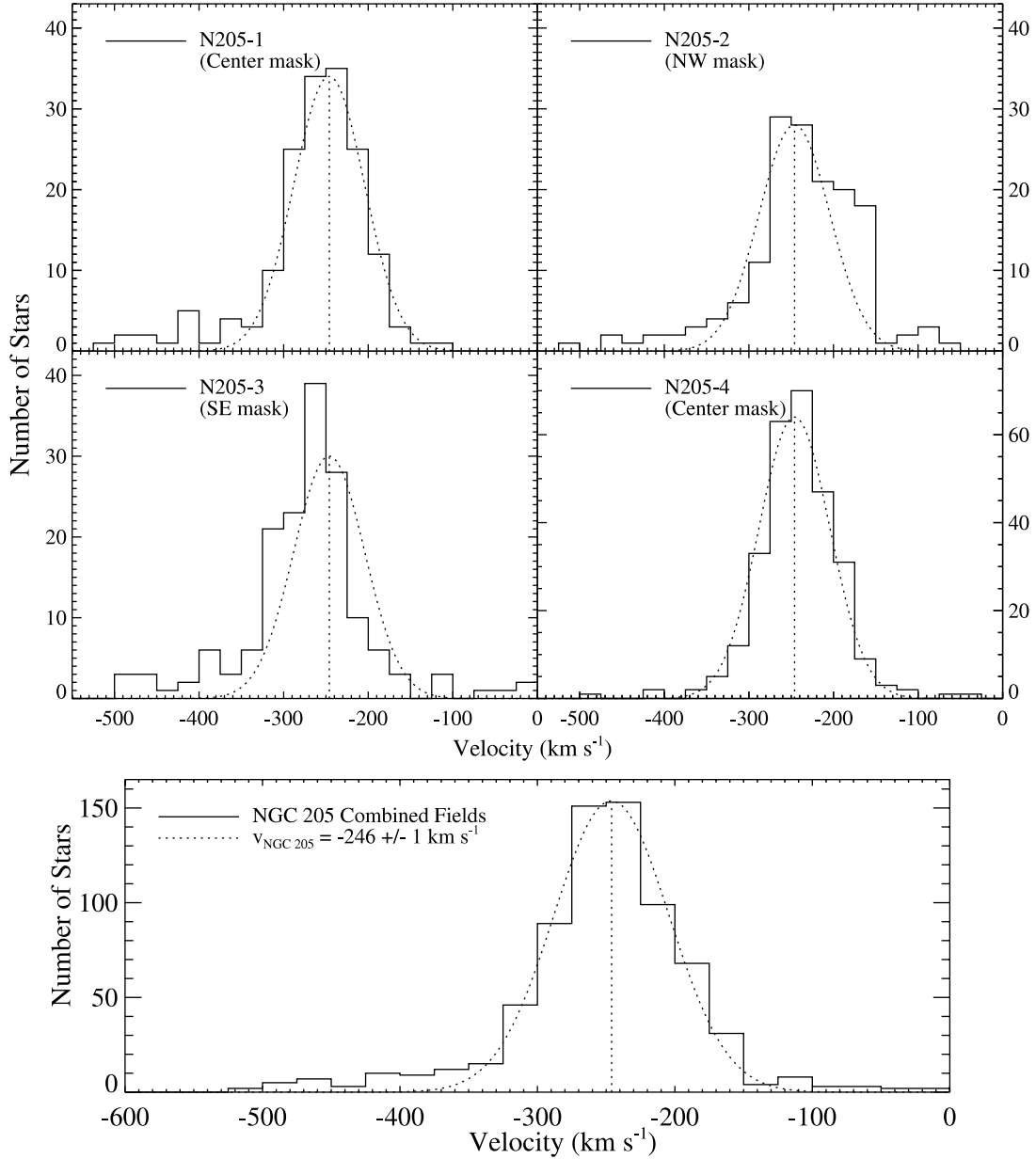


FIG. 5.—Velocity histograms for the four observed DEIMOS masks in NGC 205 (*top four panels*) and the combined fields (*bottom*). A Gaussian profile, fit to the combined velocity distribution, is plotted as the dotted curve in each panel. The Gaussian profile has a central velocity of $v_{\text{sys}} = -246 \text{ km s}^{-1}$ and a velocity width of 42 km s^{-1} . The height of the Gaussian has been scaled to the distribution of velocities in each individual panel. The masks N205-2 and N205-3, located on opposite sides of the center of NGC 205 along the major axis/tidal extension, display asymmetry in their velocity histograms toward more positive and negative velocities, respectively. This is a result of internal rotation and tidal distortion in the dE galaxy.

from our profile, excluding data beyond the tidal radius. The observed ratio for NGC 205 is $v_{\text{max}}/\sigma = 0.31$. At the ellipticity of NGC 205, the expected ratio for an oblate, isotropic, rotationally flattened body seen edge-on is slightly more than unity (Binney & Tremaine 1987). NGC 205 lies midway between a rotationally supported and anisotropic object. Interestingly, it was early kinematic observations of NGC 205 that established the paradigm that dE galaxies are supported by anisotropic velocity dispersions in contrast to rotationally supported normal elliptical galaxies (Bender & Nieto 1990). In Figure 7, we compare NGC 205 to a sample of similar-luminosity dE galaxies in the Virgo Cluster taken from Geha et al. (2003). The Virgo dE galaxies naturally fall into “rotating” and “nonrotating” categories. NGC 205 does not fall into either category, having a mixture of both rotational and anisotropic support.

At a radius of $r \sim 4'.5$, the velocity profile of NGC 205 turns over; stars beyond this radius rotate in a direction opposite that of the main galaxy body. This turnover is in the sense that stars on the side of NGC 205 closest to M31 move with more negative velocities (approaching the systemic velocity of M31) and stars on the far side move with less negative velocities. The turnover radius is coincident with the onset of isophotal twisting, as observed by Choi et al. (2002), suggesting that the outer dynamics of NGC 205 are a result of tidal stripping. We discuss further evidence for tidal interactions in § 4.

3.2. Contamination from M31 Stars and Maximum Likelihood Analysis

NGC 205 lies merely $40'$ (8 kpc) in projection from the center of M31, and our kinematic sample is likely contaminated with

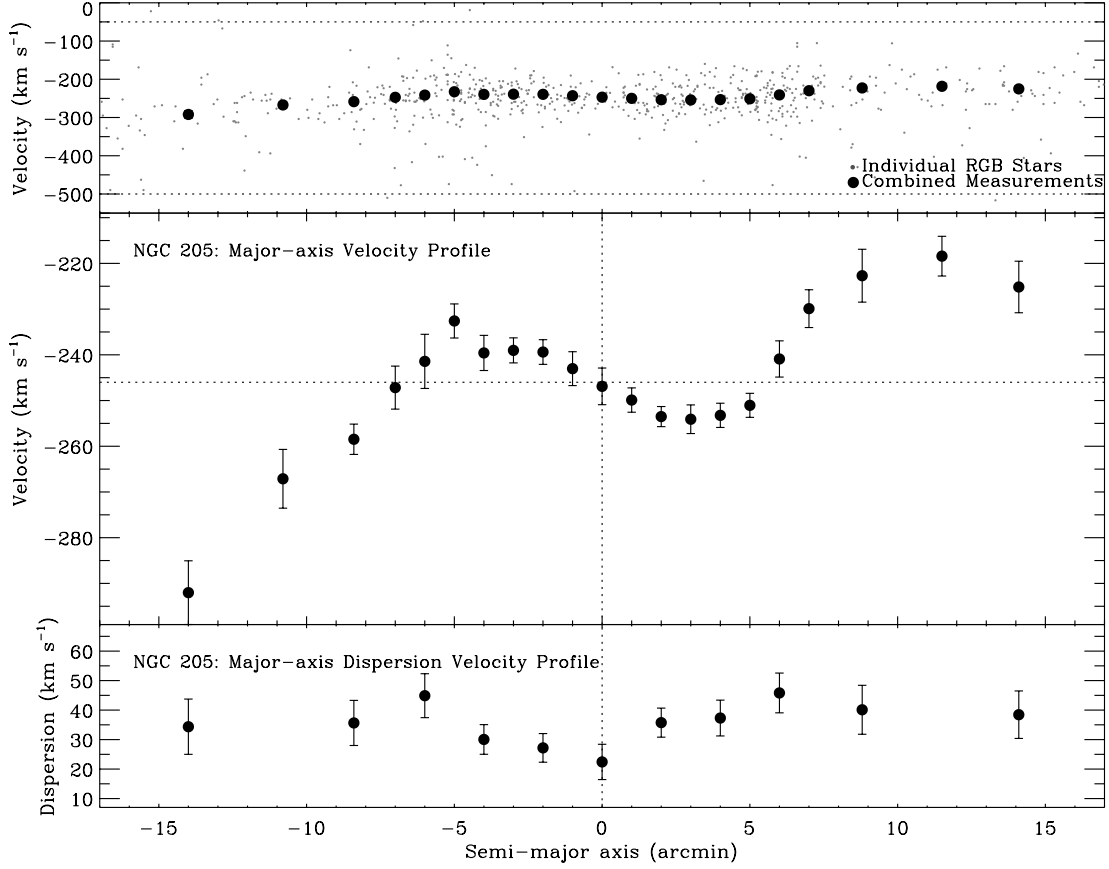


FIG. 6.—Major-axis velocity profile for NGC 205. *Top*: Small gray dots indicate Keck DEIMOS velocity measurements of individual RGB stars, and large black circles indicate the combined velocity measurements based on Gaussian fits to the velocity distribution in each radial bin. Dotted lines indicate the limits inside which the combined measurements are determined. *Middle*: Combined velocity measurements (circles) with a finer velocity scale. The vertical dotted line is plotted at the galaxy center, and the horizontal dotted line is plotted at the measured systemic velocity of NGC 205. *Bottom*: Velocity dispersion profile for NGC 205 determined using a coarser binning scheme than for the velocity profile.

TABLE 4
MAJOR-AXIS VELOCITY AND VELOCITY DISPERSION PROFILE OF NGC 205

Semimajor Distance (arcmin)	α (J2000.0)	δ (J2000.0)	v_{rot} (km s ⁻¹)	v_{err} (km s ⁻¹)	σ (km s ⁻¹)	σ_{err} (km s ⁻¹)
-17.3	00 41 12.4	+41 29 19.7	-299.1	8.9
-14.0	00 41 01.5	+41 31 25.3	-292.0	10.0	34.4	9.4
-10.8	00 40 53.5	+41 33 42.1	-267.1	9.2
-8.4	00 40 42.3	+41 34 46.9	-258.5	4.7	35.6	7.6
-7.0	00 40 32.3	+41 34 46.2	-247.2	6.7
-6.0	00 40 25.9	+41 35 08.5	-241.4	8.5	44.9	7.4
-5.0	00 40 23.9	+41 36 09.0	-232.6	5.3
-4.0	00 40 22.1	+41 37 07.0	-239.6	5.5	30.0	5.0
-3.0	00 40 23.6	+41 38 11.8	-239.0	3.9
-2.0	00 40 24.4	+41 39 12.6	-239.4	3.9	27.2	4.9
-1.0	00 40 28.4	+41 40 20.3	-243.0	5.3
0.0	00 40 30.4	+41 41 22.9	-246.9	5.7	22.4	6.0
1.0	00 40 26.3	+41 42 15.8	-249.9	3.8
2.0	00 40 21.0	+41 43 05.9	-253.5	3.1	35.7	4.9
3.0	00 40 18.9	+41 44 04.2	-254.1	4.5
4.0	00 40 23.8	+41 45 07.2	-253.2	3.8	37.3	6.1
5.0	00 40 22.3	+41 46 12.0	-251.1	3.8
6.0	00 40 24.1	+41 47 38.8	-240.9	5.7	45.8	6.7
7.0	00 40 15.1	+41 47 57.1	-229.9	5.9
8.8	00 39 58.0	+41 47 13.2	-222.7	8.3	40.1	8.3
11.5	00 39 48.7	+41 48 43.2	-218.4	6.2
14.1	00 39 36.2	+41 49 45.8	-225.2	8.1	38.4	8.0

NOTES.—The major-axis velocity and velocity dispersion profile determined from the combined measurements of individual RGB stars. Positive radial bins correspond to the northwest side of NGC 205, the side farthest from M31. The profiles are determined along the major axis of NGC 205, which forms a gentle S-curve, as shown in Fig. 3. Units of right ascension are hours, minutes, and seconds, and units of declination are degrees, arcminutes, and arcseconds.

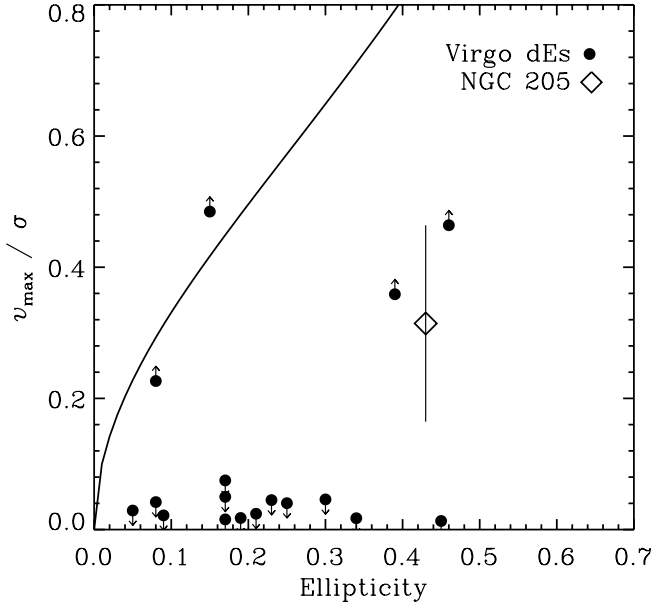


FIG. 7.—Ratio of the rotation velocity v_{\max} to velocity dispersion σ vs. mean isophotal ellipticity. The solid line shows the expected relation for an oblate, isotropic galaxy flattened by rotation. The circles indicate Virgo Cluster dE galaxies from Geha et al. (2003), and the diamond represents NGC 205. Unlike the Virgo dE galaxies, NGC 205 has a mixture of both rotational and anisotropic support.

stars associated with M31. We consider two sources for contamination, the M31 disk and halo. We estimate that contamination from M31's disk is negligible; NGC 205 lies behind M31, and its line of sight intersects the M31 disk at a point 37 kpc (7 scale lengths) along the disk from the center of M31 (assuming an inclination angle of the M31 disk of 12.5° and a disk scale length of 5.3 kpc; Walterbos & Kennicutt [1988]). At this scale length, the M31 disk surface brightness is $\mu_B = 29.2 \text{ mag arcsec}^{-2}$. In comparison, at the average radial distance of our spectroscopic

sample ($r = 5'$), the surface brightness of NGC 205 is $\mu_B = 25.4 \text{ mag arcsec}^{-2}$. Thus, our kinematic sample is unlikely to contain stars from the disk of M31.

We estimate the contamination fraction from stars in the M31 halo based on maximum likelihood fitting. We assume the M31 halo is spherically symmetric with a power-law surface brightness profile. We normalize the surface brightness of the halo at the center of NGC 205, defining the free parameter f_0 as the fractional contamination at the center of NGC 205. The M31 halo surface brightness at the position of a given slitlet i is then

$$SB_i^{\text{M31}} = f_0 SB_0^{\text{N205}} \left(\frac{r_i^{\text{M31}}}{r^{\text{M31-N205}}} \right)^\alpha, \quad (1)$$

where the angular distance between M31 and NGC 205 is $r^{\text{M31-N205}} = 40'$, the angular distance from slitlet i to the center of M31 is r_i^{M31} , and the free parameter α is the power-law index of the halo profile. The surface brightness profile of NGC 205 is based on a high-order fit to the photometry of Choi et al. (2002) with a central B -band surface brightness of $SB_0^{\text{N205}} = 19.2 \text{ mag arcsec}^{-2}$. We assume a Gaussian velocity distribution for the M31 halo with a velocity dispersion of width σ^{M31} and a systemic velocity of $v_{\text{sys}}^{\text{M31}} = -300 \text{ km s}^{-1}$ (Guhathakurta et al. 2004). Given a measured velocity of v_i for slitlet i , the probability that it was drawn from the velocity distribution of the M31 halo is

$$P_i^{\text{M31}} = \frac{1}{\sqrt{2\pi}\sigma^{\text{M31}}} \exp \left[-\frac{1}{2} \left(\frac{v_i - v_{\text{sys}}^{\text{M31}}}{\sigma^{\text{M31}}} \right)^2 \right]. \quad (2)$$

Similarly, the probability that a given velocity is drawn from the velocity distribution of NGC 205, P_i^{N205} , is the same as equation (2); however, σ^{N205} and $v_{\text{sys}}^{\text{N205}}$ are the measured quantities as a function of radius. The final probability function for each slitlet i is

$$P_i = C_i (SB_i^{\text{N205}} P_i^{\text{N205}} + SB_i^{\text{M31}} P_i^{\text{M31}}). \quad (3)$$

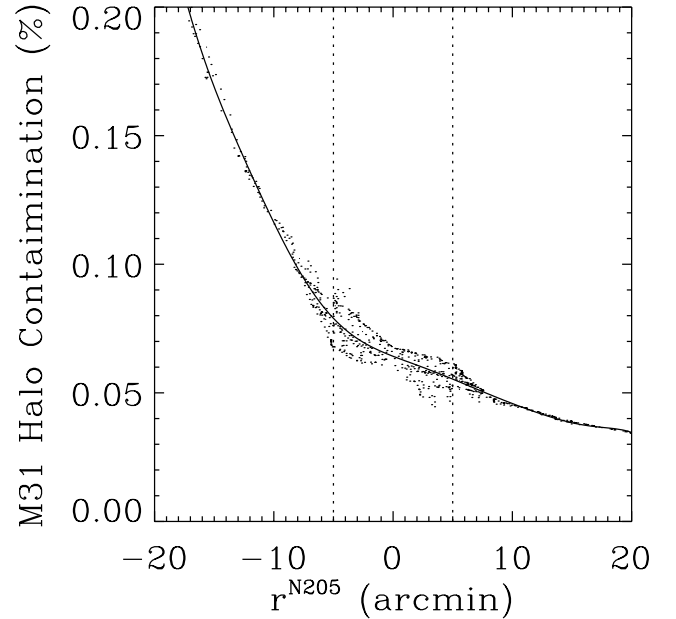
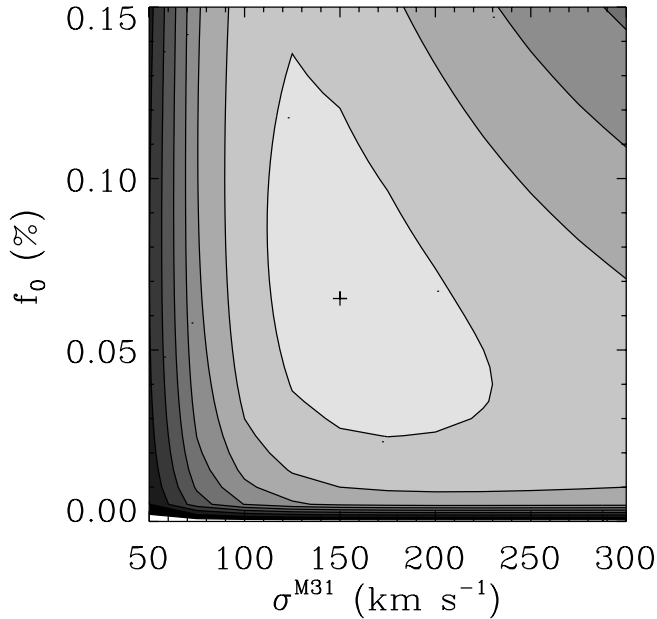


FIG. 8.—*Left*: Likelihood contours of the contamination fraction of M31 stars (f_0) vs. the velocity dispersion of the M31 halo. The third free parameter in our model, the power-law index of the M31 halo profile, is fixed at the best-fit value of $\alpha = -2.25$. The plus sign indicates the best-fitting model parameters of $f_0 = 0.065$ and $\sigma^{\text{M31}} = 150 \text{ km s}^{-1}$. *Right*: M31 halo contamination fraction as a function of position in NGC 205. The average contamination from M31 halo stars for the sample is 6.5%. The vertical dotted lines indicate the radius of the turnover in the major-axis velocity profile.

The normalization constant $C_i \equiv 1/(\text{SB}_i^{\text{NGC205}} + \text{SB}_i^{\text{M31}})$ is defined such that the integral over P_i is equal to unity. The probability P_i is evaluated for each slitlet, and the natural logarithm of this quantity is summed over all slits. We do a gridded parameter search over the free parameters f_0 , σ^{M31} , and α and maximize the function $M = \sum_i \ln(P_i)$. As shown in Figure 8 (*left*), the best-fitting parameters that maximize the quantity M are $f_0 = 0.065$, $\sigma^{\text{M31}} = 150 \text{ km s}^{-1}$, and $\alpha = -2.25$. We note that these best-fitting M31 halo parameters are in good agreement with the measured M31 halo velocity dispersion by Guhathakurta et al. (2004) and an r^{-2} halo surface brightness profile.

In Figure 8 (*right*), we plot the fractional contamination in our kinematic sample from the M31 halo as a function of distance from the center of NGC 205 using the best-fit parameters determined above. At the center of NGC 205, the best estimate of the contamination from M31 is 6%; this corresponds to 1.5 out of 25 stars per radial bin. On the side of NGC 205 closest to M31 the contamination is 20%, while on the far side the contamination is less than 3%. The average halo contamination fraction for our sample is 6.5%.

4. THE TIDAL DISRUPTION OF NGC 205

The outer dynamics of NGC 205 place significant constraints on the tidal interaction between NGC 205 and its parent galaxy, M31. While the main body of NGC 205 is rotating with a maximum velocity of 11 km s^{-1} , the major-axis velocity profile turns over abruptly at a radius of 4.5 (1 kpc); stars at larger radii are moving in the opposite direction than the main galaxy body. The turnover radius coincides with the onset of isophotal twisting (Hodge 1973; Kent 1987) and a downward break in the surface brightness profile (Choi et al. 2002). Both features have been demonstrated by Choi et al. to be hallmarks of tidal stripping. We make a simple estimate of the tidal radius of NGC 205, assuming NGC 205 and M31 to be point masses. We adopt a physical separation distance between these two galaxies of $r^{\text{NGC205-M31}} = 40 \text{ kpc}$, a mass of M31 inside this distance of $M^{\text{M31}} = 1 \times 10^{11} M_\odot$ (Geehan et al. 2005), and a total mass of NGC 205 of $M^{\text{NGC205}} = 2 \times 10^9 M_\odot$ (calculated from the maximum rotation velocity and velocity dispersion at the turnover radius). The tidal radius is calculated to be $r_{\text{tidal}} \sim 4'$ (1.0 kpc). The observed velocity turnover in NGC 205 at roughly this distance is therefore due to tidal stripping from M31; stars beyond this radius are no longer bound to NGC 205.

The stellar motion beyond the tidal radius of NGC 205 suggests that it is on a prograde encounter with its parent galaxy: the spin angular momentum vector and the orbital angular momentum vector are parallel. The eventual destruction of a satellite on a prograde orbit is expected to proceed more quickly and create

more spectacular tidal tails than one on a retrograde orbit (e.g., compare Figs. 1 and 2 of Toomre & Toomre [1972]). We calculate the timescale for the destruction of NGC 205 based on the dynamical friction timescale. Using equation (7.26) in Binney & Tremaine (1987), we assume that the orbital velocity of NGC 205 is related to the velocity difference between NGC 205 and M31 ($=\sqrt{3} \times 60 \text{ km s}^{-1}$) and calculate $t_{\text{fric}} \sim 3 \times 10^9 \text{ yr}$. Detailed dynamical modeling is required to determine whether features in the M31 halo, such as stellar substructure (McConnachie et al. 2004) or H I clouds (Thilker et al. 2004), are indeed associated with the orbit of NGC 205.

5. SUMMARY

We present the stellar kinematics of NGC 205 out to large radii based on Keck DEIMOS multislit spectroscopic observations of 725 individual red giant branch stars. NGC 205 is one of the closest examples of a dwarf elliptical (dE) galaxy and the prototype of this galaxy class. Early kinematic observations of NGC 205 established the paradigm that dE galaxies are supported primarily by anisotropic velocity dispersions (Bender et al. 1991). Although kinematic studies of dE galaxies outside the Local Group suggest that a fraction of dE galaxies are indeed supported by anisotropic velocity dispersion alone (Geha et al. 2003; De Rijcke et al. 2001), NGC 205 itself has significant rotation. We measure a maximum major-axis rotation speed for the body of NGC 205 of $11 \pm 5 \text{ km s}^{-1}$, implying that this galaxy is supported by a mixture of both rotational and anisotropic velocities.

The velocity profile of NGC 205 turns over at a major-axis distance of 4.5 (1 kpc). This turnover is due to gravitational interaction between NGC 205 and its parent galaxy, M31. The motion of stars beyond the tidal radius suggests that NGC 205 is on a prograde encounter with M31. Detailed dynamical modeling should clarify what, if any, substructure in the M31 halo is associated with disruption of NGC 205 and provide insight into the ongoing interactions between these two galaxies.

We thank S. Demers and P. Battinelli for kindly providing their photometric catalogs. We also thank P. Choi, G. Laughlin, D. Kelson, and R. P. van der Marel for productive and enjoyable conversations. M. G. is supported by NASA through Hubble Fellowship grant HF-01159.01-A awarded by the Space Telescope Science Institute, which is operated by the Association of Universities for Research in Astronomy, Inc. P. G. acknowledges support from NSF grant AST 03-07966 and NASA/STScI grant GO-10265.02. R. M. R. acknowledges funding by grant AST 03-07931.

REFERENCES

- Beasley, M., Strader, J., Brodie, J., Cenarro, J., & Geha, M. 2006, *AJ*, in press (astro-ph/0510756)
- Bender, R., & Nieto, J.-L. 1990, *A&A*, 239, 97
- Bender, R., Paquet, A., & Nieto, J.-L. 1991, *A&A*, 246, 349
- Binggeli, B., Sandage, A., & Tammann, G. A. 1988, *ARA&A*, 26, 509
- Binney, J., & Tremaine, S. 1987, *Galactic Dynamics* (Princeton: Princeton Univ. Press)
- Bullock, J. S., Kravtsov, A. V., & Weinberg, D. H. 2000, *ApJ*, 539, 517
- Cappellari, M., Bertola, F., Burstein, D., Buson, L. M., Greggio, L., & Renzini, A. 1999, *ApJ*, 515, L17
- Carter, D., & Sadler, E. M. 1990, *MNRAS*, 245, 12P
- Choi, P. I., Guhathakurta, P., & Johnston, K. V. 2002, *AJ*, 124, 310
- Corradi, R. L. M., et al. 2005, *A&A*, 431, 555
- Dekel, A., & Silk, J. 1986, *ApJ*, 303, 39
- Demers, S., Battinelli, P., & Letarte, B. 2003, *AJ*, 125, 3037
- De Rijcke, S., Dejonghe, H., Zeilinger, W. W., & Hau, G. K. T. 2001, *ApJ*, 559, L21
- Faber, S. M., et al. 2003, *Proc. SPIE*, 4841, 1657
- Ferguson, A. M. N., Irwin, M. J., Ibata, R. A., Lewis, G. F., & Tanvir, N. R. 2002, *AJ*, 124, 1452
- Font, A. S., Johnston, K. V., Bullock, J. S., & Robertson, B. 2005, in *IAU Colloq. 198, Near-Fields Cosmology with Dwarf Elliptical Galaxies*, ed. H. Jerjen & B. Binggeli (Cambridge: Cambridge Univ. Press), 126
- Freedman, W. L., et al. 2001, *ApJ*, 553, 47
- Geehan, J., Fardal, M., Babul, A., & Guhathakurta, P. 2005, *MNRAS*, submitted (astro-ph/0501240)
- Geha, M., Guhathakurta, P., & van der Marel, R. P. 2002, *AJ*, 124, 3073
- . 2003, *AJ*, 126, 1794
- Guhathakurta, P., et al. 2004, *AJ*, submitted (astro-ph/0406145)
- Haas, M. 1998, *A&A*, 337, L1
- Hodge, P. W. 1973, *ApJ*, 182, 671

- Horne, K. 1986, *PASP*, 98, 609
- Ibata, R., Chapman, S., Ferguson, A. M. N., Irwin, M., Lewis, G., & McConnachie, A. 2004, *MNRAS*, 351, 117
- Ibata, R., Irwin, M., Lewis, G., Ferguson, A. M. N., & Tanvir, N. 2001, *Nature*, 412, 49
- Ibata, R. A., Gilmore, G., & Irwin, M. J. 1995, *MNRAS*, 277, 781
- Kent, S. M. 1987, *AJ*, 94, 306
- Kleya, J. T., Wilkinson, M. I., Gilmore, G., & Evans, N. W. 2003, *ApJ*, 588, L21
- Lee, M. G. 1996, *AJ*, 112, 1438
- Mastropietro, C., Moore, B., Mayer, L., Debattista, V. P., Piffaretti, R., & Stadel, J. 2005, *MNRAS*, 364, 607
- Mayer, L., Governato, F., Colpi, M., Moore, B., Quinn, T., Wadsley, J., Stadel, J., & Lake, G. 2001, *ApJ*, 559, 754
- McConnachie, A. W., Irwin, M. J., Ferguson, A. M. N., Ibata, R. A., Lewis, G. F., & Tanvir, N. 2005, *MNRAS*, 356, 979
- McConnachie, A. W., Irwin, M. J., Lewis, G. F., Ibata, R. A., Chapman, S. C., Ferguson, A. M. N., & Tanvir, N. R. 2004, *MNRAS*, 351, L94
- Meylan, G., Sarajedini, A., Jablonka, P., Djorgovski, S. G., Bridges, T., & Rich, R. M. 2001, *AJ*, 122, 830
- Moore, B., Lake, G., & Katz, N. 1998, *ApJ*, 495, 139
- Peletier, R. F. 1993, *A&A*, 271, 51
- Peterson, R. C., & Caldwell, N. 1993, *AJ*, 105, 1411
- Schlegel, D. J., Finkbeiner, D. P., & Davis, M. 1998, *ApJ*, 500, 525
- Simien, F., & Prugniel, P. 2002, *A&A*, 384, 371
- Thilker, D. A., Braun, R., Walterbos, R. A. M., Corbelli, E., Lockman, F. J., Murphy, E., & Maddalena, R. 2004, *ApJ*, 601, L39
- Toomre, A., & Toomre, J. 1972, *ApJ*, 178, 623
- van Zee, L., Skillman, E. D., & Haynes, M. P. 2004, *AJ*, 128, 121
- Walterbos, R. A. M., & Kennicutt, R. C. 1988, *A&A*, 198, 61
- Welch, G. A., Sage, L. J., & Mitchell, G. F. 1998, *ApJ*, 499, 209
- Young, L. M., & Lo, K. Y. 1997, *ApJ*, 476, 127